*Korean J. Chem. Eng.*, 40(8), 1882-1891 (2023)
DOI: 10.1007/s11814-023-1406-2

pISSN: 0256-1115
eISSN: 1975-7220

# Sustainable production of acrolein over highly stable and selective $WO_3$ over $SiO_2$-$TiO_2$ catalysts

**Ismail Boz†, Mehtap Safak Boroglu, Yasar Zengin, and Busra Kaya**

Istanbul University-Cerrahpaşa, Faculty of Engineering, Chemical Engineering Department, Avcılar, 34320 Istanbul, Turkey
(*Received 1 October 2022 • Revised 11 February 2023 • Accepted 27 February 2023*)

**Abstract**−The effects of the addition of colloidal silica ($cSiO_2$) and solvents used in the catalyst preparation on the activity and stability of $WO_3$-$TiO_2$ catalysts are reported in this paper. The highly stable and selective $WO_3$ supported $cSiO_2$-$TiO_2$ catalysts were prepared and tested in the vapor-phase glycerol oxy-dehydration. $WO_3$-$TiO_2$ catalysts with and without $cSiO_2$ were characterized by XRD, SEM, $NH_3$-TPD, infrared spectroscopy of pyridine (FTIR-Py), XPS, RAMAN, and $N_2$ adsorption-desorption (BET). The highest medium strength acidity and optimum Brønsted to Lewis acid site ratio of $WO_3$ catalysts were achieved upon the addition of colloidal silica ($cSiO_2$) onto $TiO_2$ support. The medium strength acidity of Brønsted acid sites was responsible for the improved acrolein selectivity and stability. The other major factors in glycerol conversion and acrolein selectivity were the glycerol content and liquid hourly space velocity. The yield to acrolein was up to 70% and kept almost constant in a 50 h continuous run at 300 °C. The gradual decrease in glycerol conversion was due to the build-up of oxygen-containing carbonaceous materials deposited on the catalyst surface.

Keywords: Acrolein, Dehydration, Durability, Glycerol, $WO_3$-$SiO_2$-$TiO_2$ Catalyst

## INTRODUCTION

Biofuels, bioethanol, and biodiesel are among the sustainable resources in place of depleting nonrenewable ones. Biodiesel production, concomitantly by-product glycerol, is projected to be 50 billion liters by 2030 [1]. The steady increase in biodiesel production stimulated glycerol's conversion into more valuable fuels and chemical products [2-4]. Gas phase dehydration over solid acid catalysts is a known pathway to platform chemicals from the organic feedstock. The usage of solid acid catalysts diminishes the usage of organic solvents, harmful liquid acids, long processing times, and difficult product separation steps. Several value-added chemicals derived from glycerol, such as epichlorohydrin, propylene glycol, alkyl lactates, olefins, and acrylic acid, create an extra demand for the ever-growing market of glycerol. Acrolein is one of the chemicals obtained from glycerol with various industrial uses, including methionine, acrylic acid, propylene glycol, and various other product [3]. Acrylic acid can be produced from glycerol via acrolein synthesis step [5,6]. However, numerous problems in acrolein synthesis exist including robust catalyst design and purification of crude glycerol [7]. The other major impediments to acrolein production from glycerol are the development of non-deactivating stable solid acid catalysts and commercial viability [8-12].

Among active zeolites' catalysts, H-ZSM-5 and H-ferrierite reached acrolein yields of 53.8% and 54.6%, respectively. The surface acidity depended on the $SiO_2/Al_2O_3$ ratios [13,14]. Although zeolitic catalysts exhibit high-initial dehydration activity, they suffer from quick deactivation, predominantly due to hydrothermal instability or pore-clogging [15].

In another important group of solid acid catalysts, heteropolyacids, Tsukuda and co-workers [16] studied the influence of the textural properties of the heteropolyacids supported on porous silica in terms of acrolein selectivity. They prepared Keggin-type heteropolyacids, such as phosphotungstic acid ($H_3PW_{12}O_{40}$) or silicotungstic acid ($H_4SiW_{12}O_{40}$) on the 6-nm silica support. They achieved 100% conversion with the acrolein selectivity of 65% and 75%, respectively. They reported that the selectivity remained constant for smaller pore sizes, but the conversion decreased rapidly [16]. Solid acidity, the ratio of surface acidity types and pore structure all play prime roles in achieving good and stable performance in the sustainable production of acrolein [17]. One common defect of all these catalysts is the instability under harsh reaction conditions and rapid deactivation. Several strategies can surmount these limitations, such as in-situ regeneration by injecting oxygen, intermittent regeneration, and moving bed regeneration [18].

The development of non-deactivating, economical, stable, and selective catalysts remains a major problem in acrolein synthesis from glycerol. In this respect, mixed metal oxides are the best available and economical alternative catalysts, such as $WO_3$-$TiO_2$ [19, 20] and $WO_3$-$ZrO_2$ [21]. The active species, appropriate crystal phases and pore structure must be provided to ensure a selective, stable and economical catalyst [17]. Massa et al. [22] tested $TiO_2$, $Al_2O_3$, and $SiO_2$-supported solid acid catalysts with Nb and W additives [22]. They claimed that $Nb_2O_5$ and $WO_3$ related acid sites' concentrations were higher over $TiO_2$ and $Al_2O_3$ supports than that over $SiO_2$ support. In this study, the highest acrolein yield of 80% was obtained with a $WO_3$-$TiO_2$ catalyst. Babaei et al. [23] conducted a detailed DFT study on glycerol adsorption and the mechanism of

†To whom correspondence should be addressed.
E-mail: ismailb@iuc.edu.tr

dehydration to acrolein over the (100) surface of anatase $TiO_2$ [23]. Three possible glycerol dehydration pathways were postulated on the (100) surface of $TiO_2$ (tautomerization and dehydration etc.). They also claimed that the $TiO_2$ surface exhibited the most activity in the proton transfer reaction with 89.1 kcal/mol activation in the third path for producing acrolein.

Industrial processes often dictate one stage production for glycerol dehydration to acrolein and the subsequent oxidation to acrylic acid over typically Mo-based catalysts [24]. The partial oxidation of acrolein in propylene route is well understood and applied on an industrial scale. We focused on the development of non-deactivating, durable and active catalysts for the selective dehydration of glycerol to acrolein.

The main objective of this study was to elucidate the effects of colloidal silica addition and solvents used in the preparation of selective and stable $WO_3$-$TiO_2$ catalysts. We aimed to enhance the total surface area by the addition of colloidal silica and an appropriate choice of solvents used in the preparation of catalysts. We intended to avoid supports with delicate pore structures prone to quick deactivation. The relationship between the surface properties and catalytic acidity of $WO_3$-$cSiO_2$-$TiO_2$ catalyst samples was screened by extensive characterization techniques. We also examined the relationship between the catalytic performance (conversion, selectivity, stability) and physico-chemical properties, such as surface acidity and acid types.

## EXPERIMENTAL

### 1. Catalyst Preparation

The ammonium metatungstate (AMT) was impregnated onto $TiO_2$ in anatase form with or without the epoxy silane-modified colloidal silica ($cSiO_2$) (Levasil cc301, by nouryon). Titanium dioxide, AN100 anatase, was supplied from a local distributor and manufactured by Nanjing Titanium Dioxide Chemical Co., Ltd. AMT source was Alfa Aesar chemicals (Cat No 44792). Oxalic acid was of food grade and sourced from a local supplier. Oxalic acid was also added as pore making agent. Silica content was kept constant at 10% by weight to $TiO_2$. $TiO_2$ particles were wet milled with 3-mm $ZrO_2$ ball mills for 24 h at 200 rpm. The particle size was reduced to an average of 1.7±1.3 μm. The surface charges of support $TiO_2$ particles were changed to facilitate the adsorption and dispersion of AMT. Additional concentrated $H_2SO_4$ was used together with oxalic acid to reduce the pH of the $TiO_2$ suspension below 2. Four different AMT precursor impregnation solutions, namely, Oxalic acid +acidified water (OA imp. W), Oxalic acid +acidified water/ethyl alcohol (50 : 50 v/v) mixture (OA imp. W/EA), Oxalic acid +acidified alcohol (OA imp. EA), without oxalic acid in acidified water alone (Imp. W), were used in the synthesis. $WO_3$ nominal loadings changed from 5 to 30 wt%. A mechanical stirrer-heater vigorously mixed the suspension at around 80 °C until all water was evaporated. Dried samples were calcined at 550 °C for 4 h under flowing air. The typical resulting material was nominally denoted as 5 to 30 wt% $WO_3$-(with or without $cSiO_2$)-$TiO_2$ ((OA imp. W), (OA imp. W/EA), (OA imp. EA) and (Imp. W)).

### 2. Catalyst Characterization

Powder X-ray diffraction patterns were recorded on a Rigaku D/Max 2200 diffractometer with CuK$\alpha$ radiation ($\lambda$=1.5418 A, at 30 kV and 30 mA) in the range of 10 to 80 with a hollow fiber monochromator. Surface area, pore size, and pore volume were all measured and calculated from nitrogen adsorption-desorption isotherms using a micromeritics multipoint BET analyzer. Samples were degassed at 300 °C for 2 h. BET, BJH and t-plots were used for further calculations.

The particle size distribution of samples was measured using a Brookhaven 90 Plus Nano Particle Size Analyzer. Before the particle size measurement, the sample was prepared at 0.1% concentration in deionized water containing Triton X-100 (t-Oct-$C_6H_4$-$(OCH_2CH_2)_xOH$, x=9-10, CAS Number: 9002-93-1) and mixed in an ultrasonic bath.

Before pyridine adsorption, samples were ground to below 200-mesh sieve and dried in a forced flow high-temperature oven at 400 °C for 4 h. A dry seal vacuum desiccator containing the samples and pyridine in separate shallow glass beakers was placed in an oven kept at 60 °C. The pyridine beaker was removed from a vacuum desiccator and pyridine-loaded samples in shallow glass beakers were heated to 150 °C for 6 hours to remove physically adsorbed pyridine.

Pyridine FTIR spectroscopy analysis of the samples was recorded by absorption infrared (IR) radiation technique using a Thermo Nicolet 380 FTIR Smart Diffuse Reflectance accessory between 4,000 and 650 $cm^{-1}$.

SEM measurements were performed using a Zeiss Ultra Plus field emission scanning electron microscope. An SE2 detector was used to obtain the pictures. 5.00 kV acceleration voltage and 5.0-5.1-mm working distance were set.

XPS spectra of $WO_3$/$TiO_2$ samples were taken by a Thermo Scientific K-Alpha spectrometer using an aluminum anode (AlK$\alpha$ = 1,468.3 eV) at an electron take-off angle of 90° (between the sample surface and the axis of the analyzer lens). The spectra were recorded using an Advantage 5.9 data system. The binding energy scale was calibrated by assigning the adventitious C 1s signal at 284.8 eV.

### 3. Catalytic Reaction

The vapor phase glycerol dehydration reactions were carried out under atmospheric pressure in a stainless steel fixed bed reactor (with 7.5 mm inner diameter) in the range of 250-325 °C. The reactor setup is equipped with 2 mass flow controllers (Brooks, 5850 TR), an accurate syringe pump controlling the liquid feed flow (Üzümcü, SP 01), and a condenser on the product line. Before each experiment, the reactor setup including the catalyst samples was heated at 300 °C for 30 min, under a 45 ml/min flow of nitrogen. The aqueous feed stream, 10 wt% glycerol in water, was fed into the reactor at a rate of 7.2-28.8 ml/h. The reactant feed was a mixture of glycerol/water/oxygen/nitrogen with various molar ratios adjusting the glycerol/oxygen molar ratio to 2/5. In a typical experiment, the reactor bed was filled with 0.05-1.50 g catalyst, glass wool, and quartz particles (0.1-0.5 mm). For the optimization studies, catalyst particle size and bed height, the feed flow rate and the catalyst diluent effect were also explored in the reactor setup.

The glycerol conversion ($X_{Gly}$) and product selectivity ($S_i$) were calculated in accordance with Eqs. (1) and (2).

$$X_{Gly}(\%) = \frac{n_{Gly_{input}} - n_{Gly_{output}}}{n_{Gly_{input}}} \times 100 \quad (1)$$

$$S_i(\%) = \frac{n_i}{n_{Gly_{input}} - n_{Gly_{output}}} \times \frac{Z_i}{Z_{Gly}} \times 100 \quad (2)$$

$n_{Gly_{input}}$ and $n_{Gly_{output}}$ are the molar flow rates of glycerol in input flow and effluent flow (mol/min), $n_i$ is the molar flow rate of $i^{th}$ component in the condensable effluent. Z represents the number of carbon atoms of components. Carbon balances and mass balances between the mass of input and condensables in effluent were checked every 2 h of time-on-stream by weighing the condensed liquid and analyzed by an offline gas chromatograph. The carbon balance calculations are based on the condensable products collected in the condenser. The progress in the amount of the condensable is also shown in some activity graphs along with time on stream results and in the activity tables.

For a few selected experiments, amounts of oxygen and $CO_x$ were followed by an online GC after effluent passed from a condenser. Since the oxygen was constantly fed at a high molar ratio (typically glycerol/$O_2$ molar ratio of 1 to 2.5) throughout the reaction, hence oxygen was barely consumed (<1%). The amount of $CO_x$ in gaseous effluent was always detected in small quantities; therefore, the $CO_x$ yield analysis was not followed in the further experiments.

The reaction products and unconverted reactants were collected in a condenser kept at −2 °C. The liquid samples were collected hourly, filtered, and analyzed by an off-line gas chromatograph (Model 6890N, AGILENT) equipped with an autosampler, a capillary column (INNOWAX, 30 m, 0.32 mm, 0.50 μm), and an FID detector. The gaseous products were analyzed by an online GC (Model 6890N, AGILENT), equipped with an FID (HP-PLOT $Al_2O_3$/KCl column, 30 m*0.53 mm*15 μm) and a TCD (Poraplot Q column, 30 m*0.53 mm*40 μm and a Molecular Sieve 5A column, 30 m*0.53 mm*50 μm). Before each liquid sample injection, 0.1 ml of n-butanol ($C_4H_{10}O$, >99% purity, CAS Number: 71-36-3) as an internal standard was added to the analyte solution. The procedure used in the analysis of liquid samples is as follows: 300 °C inlet temperature, 6 min waiting at 60 °C, heating up to 150 °C with 10 °C/min speed, 8 min waiting, heating up to 240 °C with 20 °C/min speed for oven temperature and 250 °C for FID temperature.

## RESULTS AND DISCUSSION

### 1. Characterization of the Catalysts

Powder XRD diffractograms of (a) 5%, (b) 10%, (c) 15%, (d) 20%, and (e) 30%$WO_3$-c$SiO_2$-$TiO_2$ samples are shown in Fig. 1. The crystallographic phase of $WO_3$ did not change at all with various loadings. At low loadings of 5%$WO_3$, peaks reflecting monoclinic $WO_3$ are merely visible, as loadings increased from 10% up to 30%, the crystallinity of $WO_3$ peaks is increased too. The diffraction patterns show only peaks of $TiO_2$ in anatase phase and $WO_3$ in monoclinic phase.

Fig. S1 exhibits the powder XRD patterns of (a) pure colloidal $cSiO_2$ sample, 15%$WO_3$/$cSiO_2$, fresh (b), and used (c) in oxy-dehydration reactions after 8 h. For the pure $cSiO_2$ sample, an amorphous phase's peak at $2\theta$=22.6° corresponding to the colloidal silica is detected as shown in Fig. S1(a). Music et al. [25] prepared amorphous $SiO_2$ by the sol-gel procedure. In their work, an amorphous silica peak is centered at $2\theta$=23°, which coincides with the peak position detected in this study.

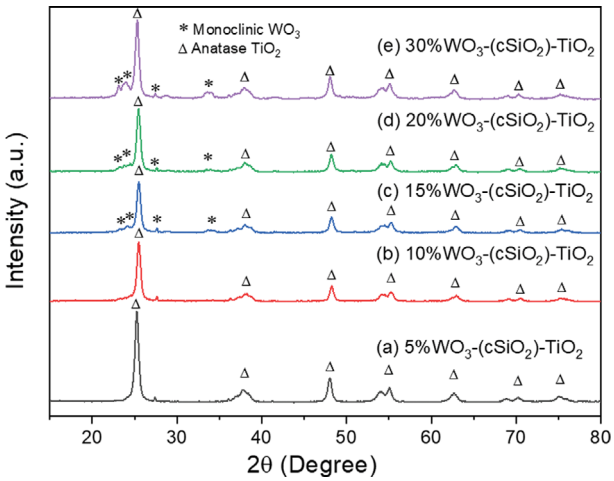


**Fig. 1. XRD patterns of fresh samples (a) 5%, (b) 10%, (c) 15%, (d) 20%, and (e) 30%$WO_3$-(c$SiO_2$)-$TiO_2$.**

From Fig. S1(b), $2\theta$=23.10, 23.70, 24.20, and 34.10° values reflecting to crystalline patterns of (002), (020), (200) and (202) are of the monoclinic phase of $WO_3$ (JCPDS no=43-1035). Monoclinic $WO_3$ phase is crystallized with relatively strong and sharp peaks. After 8 h of reaction at 300 °C, there is no change in the $WO_3$ crystal phase and crystallinity as well. From these patterns, the structure of $cSiO_2$ calcined at 550 °C corresponds to the amorphous silica. It is observed from Fig. S1(c) that the used catalysts exhibited well-defined characteristic peaks of monoclinic $WO_3$ and amorphous $cSiO_2$. Moreover, it is noted that $cSiO_2$ merely acted as an inert high surface area support.

XRD patterns of anatase $TiO_2$ sample without $cSiO_2$ additive (a), fresh 15%$WO_3$-$TiO_2$ (b) and used (c) in 8 h oxy-dehydration reaction are shown in Fig. S2. A powder X-ray diffraction pattern of $TiO_2$ dried and calcined for 2 h at 500 °C is also demonstrated in Fig. S2(a). The characteristic crystalline peaks of $2\theta$ (hkl)=25.27° (101), 48.01° (200), 53.85° (105), 55.03° (211) corresponding to the anatase phase of $TiO_2$ (JCPDS: 21-1272) are observed in all XRD patterns. As can be seen from the XRD diffractograms in Fig. S2, $TiO_2$ nanoparticles in the anatase phase exhibit a high intensity of characteristic peaks. The monoclinic $WO_3$ peaks that could be observed after 15% loading, exhibit a lower intensity, which is taken as an indication of a very homogeneous distribution on the surface.

XRD diffraction peaks at $2\theta$ (hkl)=23.10° (002), 23.70° (020), 24.20° (200), and 34.10° (202) shown in Fig. S2(b) are clearly distinguishable and correspond to monoclinic phase crystals of $WO_3$ (JCPDS: 43-1035). It is noteworthy that the characteristic diffraction peaks of monoclinic $WO_3$ particles are visible, albeit at a very low intensity, compared to the characteristic peaks of anatase $TiO_2$. After 8 h of dehydration reaction at 300 °C, the incorporation of $WO_3$ possibly led to a slight distortion in the matrix of $TiO_2$ anatase phases (see Fig. S2(c)). However, there is only a 0.3 degree shift at this relatively low reaction temperature, although the change may be attributed to the weak interaction between $WO_3$ and $TiO_2$ support. This interaction is observed by the decrease in crystal size after the dehydration reaction, which is calculated as 50 nm in the

**Table 1. Specific surface areas, pore volumes, pore widths and acidity of $WO_3$/$cSiO_2$-$TiO_2$ catalysts**

| Catalyst | $S_{BET}$[a] ($m^2$/g) | Pore volume[b] ($cm^3$/g) | Average pore width[c] (nm) | Crystal size, nm, fresh | Crystal size, nm, used | B/(B+L), DRIFT FTIR (pyridine) | Low-strength acidity[d] (μmoles $NH_3$/g) | Medium strength acidity[e] (μmoles $NH_3$/g) | High-strength acidity[f] (μmoles $NH_3$/g) |
|---|---|---|---|---|---|---|---|---|---|
| $cSiO_2$ | 255 | 0.17 | 2.76 | - | - | 0.40 | 99 | 27 | 44 |
| $TiO_2$ | 10 | 0.01 | 4.90 | 42 | - | 0.30 | 380 | 372 | 84 |
| 5%$WO_3$-$TiO_2$ | 84 | 0.15 | 6.94 | 30 | 28 | 0.52 | 515 | 366 | 242 |
| 10%$WO_3$-$TiO_2$ | 79 | 0.13 | 6.89 | 27 | 28 | 0.68 | 800 | 667 | 125 |
| 15%$WO_3$-$TiO_2$ | 62 | 0.11 | 6.66 | 25 | 26 | 0.74 | 947 | 1,437 | 843 |
| 15%$WO_3$-$TiO_2$ (w/o $cSiO_2$)[g] | 10 | 0.01 | 4.90 | 50 | 41 | 0.49 | 623 | 568 | 89 |
| 20%$WO_3$-$TiO_2$ | 63 | 0.11 | 6.70 | 27 | - | 0.70 | 760 | 1,517 | 372 |
| 30%$WO_3$-$TiO_2$ | 61 | 0.11 | 6.58 | 27 | - | 0.64 | 923 | 1,278 | 157 |

[a]Measured using the BET method, [b,c]measured by BJH adsorption, [d]Low-strength 150-250, [e]Medium strength 250-400, [f]High-strength 400-600 measured by $NH_3$-TPD-MS, [g](w/o $cSiO_2$) without $cSiO_2$, - not measured.

fresh sample, but 41.4 nm in the used sample (see Table 1).

Powder XRD patterns of 15% $WO_3$ deposited onto $cSiO_2$-$TiO_2$ catalysts are shown in Fig. S3. From Fig. S3(a) of fresh 15%$WO_3$ deposited onto $cSiO_2$-$TiO_2$ catalysts, peaks at $2\theta$(hkl)=23.10° (002), 23.70° (020), 24.20° (200) and 34.10° (202) are distinguished that correspond to the monoclinic phase $WO_3$ crystals (JCPDS no.= 43-1035). Fig. S3(b) shows a slight right shift in the anatase $TiO_2$ peaks, suggesting a weak interaction between $WO_3$ and $TiO_2$ after 8 h long oxy dehydration reaction. However, the crystal size of 15%$WO_3$-($cSiO_2$)-$TiO_2$ catalysts remained relatively unchanged as listed in Table 1 (25 nm for fresh and 26 nm for used one). Hence, $cSiO_2$-$TiO_2$ samples exhibit fewer changes in crystal size, probably due to the presence of colloidal silica support. Also, $SiO_2$ doping of $TiO_2$ anatase catalysts had a similar inhibitory effect in SCR de$NO_x$ catalysts [26].

It is observed that the anatase $TiO_2$ peaks become less crystalline in the $cSiO_2$ added samples, compared to the samples without $cSiO_2$ (see Table 1). Additionally, the interactions between $WO_3$ and anatase $TiO_2$, and the shifts in $TiO_2$ peak positions, differ with respect to the presence or absence of $cSiO_2$. Accordingly, this phenomenon was reported to be the extension of the $TiO_2$ lattice diffusion pathway for $W^{n+}$ species with $cSiO_2$ contribution, thereby reducing the stress induced by $W^{6+}$ diffusion in anatase structures [27].

PXRD patterns of catalysts prepared with four different solvent mixtures are shown in Fig. 2. The effects of acidification and solvent type in the crystallization and dispersion are studied in 15%$WO_3$ loaded onto a $cSiO_2$-$TiO_2$ support system. 15%$WO_3$ loading was assertively selected to make the effects of $WO_3$ loading visible. In all solvent mixtures, the peaks reflecting $WO_3$ and $TiO_2$ are clearly distinguished. However, one striking feature of these patterns is that, in alcohol water mixture (OA imp W/EA) solvent system, peaks are much broader than those of others. This is an indication of better dispersion of monoclinic $WO_3$ onto a $cSiO_2$-$TiO_2$ support with the alcohol water mixtures.

The surface area, pore volume, average pore width and acidity of the catalysts are listed in Table 1. A high surface area of 255 $m^2$/g is observed in the case of pure $cSiO_2$. 10 wt% $cSiO_2$ with respect

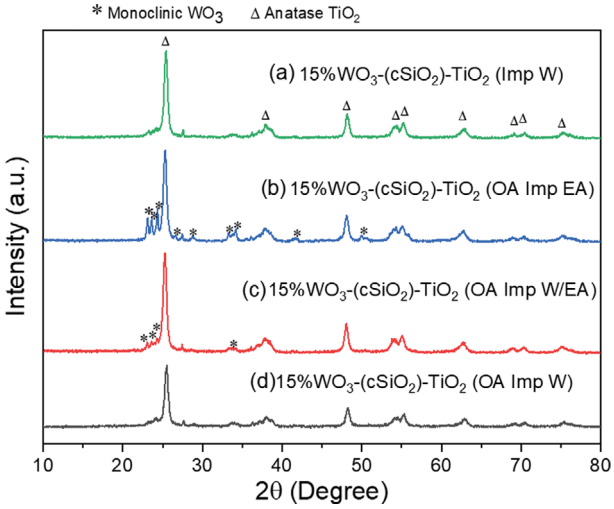


**Fig. 2. XRD patterns of the catalysts (15%$WO_3$-($cSiO_2$)-$TiO_2$) prepared with various solvent mixtures. (a) (Imp. W), (b) (OA imp EA), (c) (OA imp W/EA), (d) (OA imp W).**

to $TiO_2$ support is used in all catalysts unless otherwise stated, such as the one labeled as 15%$WO_3$-$TiO_2$ (w/o $cSiO_2$). The surface areas of $WO_3$-$TiO_2$ with 10% $cSiO_2$ apparently reduced from 83 $m^2$/g for 5%$WO_3$-$TiO_2$ to 61 $m^2$/g for 30%$WO_3$-$TiO_2$. The prominent effect of $cSiO_2$ addition is that added $cSiO_2$ provided extra surface area for the same $WO_3$ loading. BET surface areas for 15%$WO_3$-$TiO_2$ and 15%$WO_3$-$TiO_2$ (without $cSiO_2$) are 62 $m^2$/g and 10 $m^2$/g, respectively. Pore widths for the catalysts are changed between 2.76 and 6.94 nm in line with the changes in surface areas. Similarly, pore volumes for all catalysts are in the range of 0.0114-0.1671 $cm^3$/g.

The presence of $cSiO_2$ strongly increased the surface area of $TiO_2$ with respect to $TiO_2$ without $cSiO_2$. There are specific trends observed in the BET surface areas, pore size, and pore volume of the catalysts. As the $WO_3$ loading percentage is increased, crystalline tungsten oxide clusters are formed over the amorphous silica support ($cSiO_2$), thereby reducing the total surface area of the cata-

**Table 2. Acid strength distribution and B/(B+L) ratios over the catalysts prepared with various solvent mixtures**

| Catalyst | Total acidity[a] (μmoles $NH_3$/g) | Low-strength acidity[b] (μmoles $NH_3$/g) | Medium strength acidity[c] (μmoles $NH_3$/g) | High-strength acidity[d] (μmoles $NH_3$/g) | B/(B+L) DRIFT FTIR (pyridine) |
|---|---|---|---|---|---|
| 15%$WO_3$-$TiO_2$ (OA imp. W) | 1,047 | 364 | 486 | 197 | 0.74 |
| 15%$WO_3$-$TiO_2$ (OA imp. W/EA) | 2,649 | 760 | 1,517 | 372 | 0.74 |
| 15%$WO_3$-$TiO_2$ (OA imp. EA) | 1,361 | 482 | 529 | 350 | 0.56 |
| 15%$WO_3$-$TiO_2$ (imp. W) | 1,138 | 442 | 429 | 266 | 0.61 |

[a]Total acidity, [b]Low-strength 150-250, [c]Medium strength 250-400, [d]High-strength 400-600, all measured by ammonia ($NH_3$) TPD-MS

lyst. Surface areas of $WO_3$-$TiO_2$ samples are much larger than those of pure $TiO_2$ since the addition of $WO_3$ and especially $cSiO_2$ provided the additional excess surface areas. A similar increase in the surface areas after the addition of 5%$SiO_2$ was reported in $V_2O_5$/$WO_3$-$TiO_2$ de$NO_x$ catalysts [26]. For instance, 5%$SiO_2$ addition to $V_2O_5$/$WO_3$-$TiO_2$ catalysts calcined at 650 °C increased the BET surface area from 8.5 to 45.8 $m^2$/g as well as a dramatic increase in pore volume from 0.023 to 0.254 $cm^3$/g. In addition to the beneficial effect of increased surface area, Liu et al. [26] considered the inhibiting role of $SiO_2$ over $WO_3$-$TiO_2$ because of the $Si^{4+}$ incorporation into the $TiO_2$ lattice. Their calculated lattice parameters and cell volumes from XRD experiments support this conclusion. However, since the calcination temperatures used in our study are comparatively lower, we observed neither any distinct change in the lattice parameters of $TiO_2$ nor phase changes as listed in Table 2. Without the addition of $cSiO_2$ resulted in higher crystallite sizes of 50 nm, whereas, on average, the samples with $cSiO_2$ provided an average crystallite size between 25 and 30 nm. Thus, this is an indication that $cSiO_2$ facilitated the dispersion of $WO_3$ and the decrease of crystal growth too.

The surface acidities are measured by pyridine adsorption FTIR and temperature programmed desorption of ammonia (TPD-$NH_3$) and listed in Table 1. The desorption curves of $NH_3$ between 150 °C and 600 °C are deconvoluted into three distinct regions. Deconvoluted peaks between 150 and 250 °C are summed and labeled as low-strength acid sites. The peaks between 250 °C and 400 °C are labeled as medium-strength acid sites. The peaks above 400 °C are labeled as high-strength acid sites (see also Fig. S4(a)). Increasing $WO_3$ loadings resulted in a significant increase in acidity and showed a maximum in medium strength acidity up to 15%$WO_3$-$TiO_2$, and then onwards decreased (see also Fig. S4(b)). The total acidity increased in the order of increasing $WO_3$ loadings and resulted in a maximum at 15%$WO_3$-$TiO_2$ catalyst.

Total acidity and various acid strengths derived from TPD-$NH_3$ and pyridine DRIFT analysis are listed in Table 2. Four different catalyst preparation procedures led to the changes in the concentrations of medium-strength and total acidity for the various loadings between 5%-30%$WO_3$. 15%$WO_3$-$TiO_2$ prepared in oxalic acid +acidified water/ethyl alcohol (50 : 50 v/v) solvent mixture (OA imp. W/EA) resulted in almost twice the total acidity and triple medium strength acidity. However, changing solvent mixtures did not have such a distinct effect on the B/(B+L) ratios. The glycerol conversion is almost quantitative for all catalyst samples. On the other hand, selectivity to condensable products and acrolein also showed a maximum in the samples prepared by oxalic acid +acidified water/ethyl alcohol (50 : 50 v/v) mixture (OA imp. W/EA).

The beneficial effects of changing solvents in the catalytic performances are due to the higher medium strength acidity and B/(B+L) ratio. In fact, the catalyst (OA imp. W/EA) with a higher amount of medium strength acid concentration and surface area is the more active, durable and selective for oxy-dehydration of glycerol than that of those prepared in other solvent systems. Moreover, from the FTIR-pyridine graphs in Fig. S5(a) and S5(b), in addition to the high Brønsted site concentration of the 15%$WO_3$-$TiO_2$ (OA imp. W/EA) sample, the Lewis+Brønsted site concentrations are also higher than all other samples. Thus, we adopted the route based on oxalic acid +acidified water/ethyl alcohol (50 : 50 v/v) solvent mixture (OA imp. W/EA).

The morphology of a representative 15%$WO_3$-$TiO_2$ (OA imp. W/EA) catalyst by scanning electron microscopy (SEM) is shown in Fig. S6(a), (b), (c). Small, agglomerated particles with average diameters of 1.7 micrometers are clearly distinguished in Fig. S6(a) and S6(b). At higher magnifications (50K X) in Fig. S6(c), by looking at the contrast of the discrete particles, homogeneous and porous surface structure are detected.

X-ray absorption spectroscopy (XPS) was performed on 5% and 15%$WO_3$-$TiO_2$ (OA imp. W/EA) catalysts before and after 8 h of reaction. The general scan XPS spectra of Ti 2p, Si 2p, and W 5f and 7f for 5%$WO_3$-$TiO_2$ and 15%$WO_3$-$TiO_2$ catalysts before and after 8 h of reaction are depicted in Fig. S7. Typical spin splitting peak of Ti $2p_{1/2}$ is observed with 5.8 eV higher binding energies for 5%$WO_3$-$TiO_2$. At 15%$WO_3$-$TiO_2$ loadings, Ti $2p_{3/2}$ peak at 458.18 eV (fwhm=1.19), whereas, after the reaction, peak is positioned at 457.92 eV (fwhm=1.18) [27]. $TiO_2$ in anatase form is the only phase observed in agreement with the crystallographic phases detected by XRD. $WO_3$-$TiO_2$ (20 : 80) catalysts calcined at 600 °C led to the formation of rutile phase. This change in phase was explained by the incorporation of $W^{n+}$ into $Ti^{4+}$ in $TiO_2$ lattice, thereby causing stress induced in the structure of anatase by $W^{6+}$ diffusion [27-29]. However, in this study, we did not observe such phase transformation and we believe that this is due to the stabilizing effect of $cSiO_2$ addition and lower calcination temperature in line with literature findings [26]. It is worth reiterating that the addition of colloidal silica ($cSiO_2$) served in two ways. It provided a higher surface area and acted as a barrier between $WO_3$ and $TiO_2$, thus prolonging the diffusion path for $W^{n+}$ species.

From Fig. 3(a) and 3(b), similar patterns are observed for the

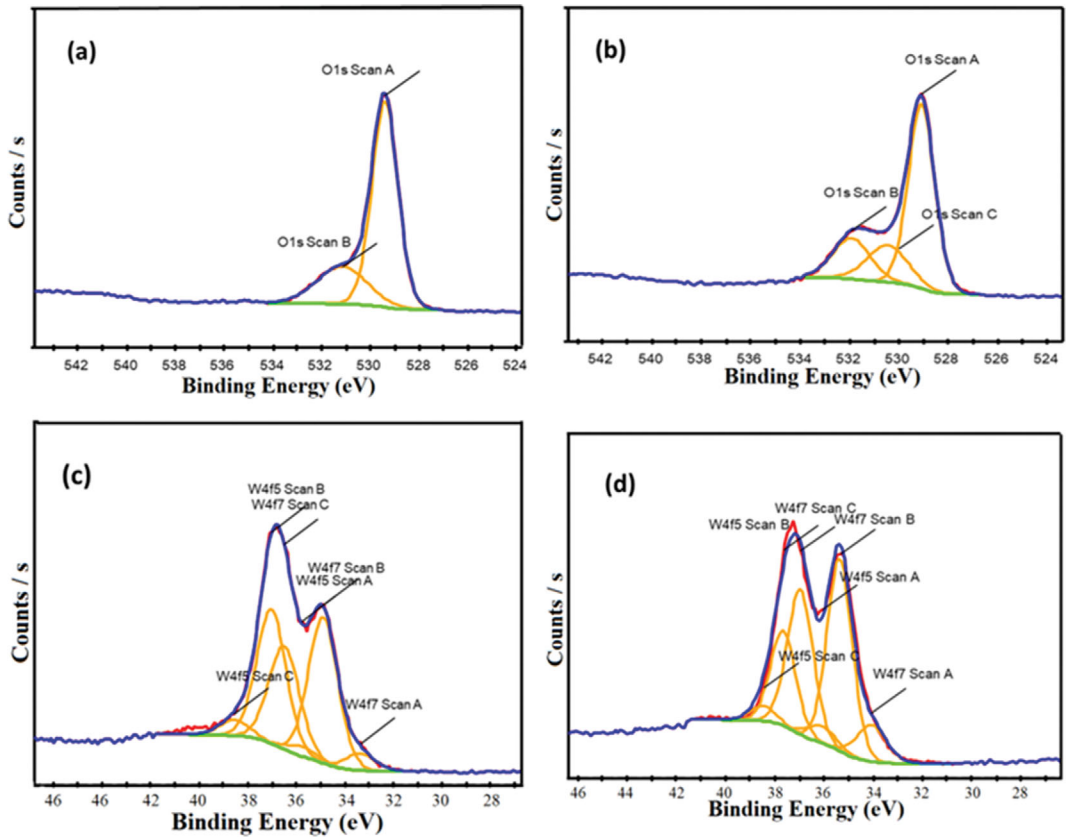


**Fig. 3. XPS spectra of W and O1s in 15%$WO_3$-$TiO_2$ catalyst before and after 50-h of reaction.**

deconvoluted O1s peaks. O1s peak for fresh 15%$WO_3$-$TiO_2$ catalyst is observed at 529.05 eV (fwhm=1.18). However, a peak belonging to oxygen-containing organic species is observed in O1s peaks for used 15%$WO_3$-$TiO_2$ catalysts, (Fig. 3(b)). O1s peaks are deconvoluted to three types of oxygen; the oxygen bound to tungsten at 529.09 eV and the oxygen bound to Ti at 530.47 eV and oxygen bound to oxygen-containing organic species at 531.93 eV. Normally -OH peaks of water are found at higher binding energies (around 534.30 eV) than oxygen-containing organic species [30]. Such peaks of -OH groups are not detected since heavy liquefied condensation products of glycerol and aldehydic species are competitively adsorbed on the surface rather than water vapor at 300 °C operating temperature. An accompanying fivefold increase in the C 1s peak is observed too. This is an indication of the presence of oxygen-containing organic species and precursors leading to the build-up of oxygenated carbonaceous species as shown in Fig. S7(c) and S7(d).

From the changes in oxygen peaks and tungsten peaks, $W^{5+}$ species in excess are not beneficial in the formation of acrolein. An equilibrium between $W^{4+}$ and $W^{5+}$ seemed to be necessary.

Fig. 4 shows Raman spectra (RS) of P25 $TiO_2$, 5%, 10%, 15%, 20%, 30%$WO_3$-$TiO_2$ (OA imp. W/EA) samples. Peak positions for first-order Raman modes of rutile, anatase, and monoclinic $WO_3$ are determined from Lorentzian fit. As shown in Fig. 4, major vibrational peaks centered at 395.9, 517, and 639.9 $cm^{-1}$ are assigned to the B1g(1), (A1g+B1g(2)), and Eg(3) vibration modes. All these vibration modes correspond to anatase crystalline phase. Peaks of

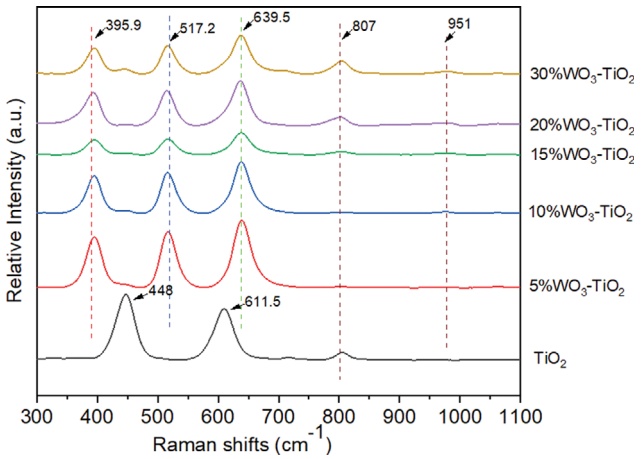


**Fig. 4. Raman spectra of 5%$WO_3$-$TiO_2$ (P25), 5, 10, 15, 20, and 30%$WO_3$-$TiO_2$ samples.**

P25 titania (mixture of rutile and anatase) are also visible at bands of 611.5, and 448 $cm^{-1}$ as shown in Fig. 4 [29,31]. We have on purpose included a titanium dioxide composed of rutile and anatase to distinguish the absence of rutile in our catalysts. Moreover, albeit broad and weak, the band at 1,095 $cm^{-1}$ is assigned to Si-O-Si stretching of the silica support.

At all loadings of $WO_3$, from 5 to 30%$WO_3$/$TiO_2$, peaks found at the band of 807, and weak shoulders at 714, and at 276 $cm^{-1}$ of crystalline $WO_3$ are assigned to W=O stretching, W=O bonding

and W-O-W deformation modes, respectively [32]. Raman spectrum shows a broad peak centered at 935 $cm^{-1}$ of tetrahedral coordinated tungsten oxide species. As the loading increased from 5% to 30%, W=O stretching normally found at 935 $cm^{-1}$ now shifted to 951 $cm^{-1}$. This shift is assigned to the presence of octahedral coordinated two dimensional polytungstate species. At relatively high loadings of $WO_3$, we now observe the presence of crystalline $WO_3$ and polytungstate species [32]. Two bands appearing in the Raman spectra at 807 and 714 $cm^{-1}$ are characteristic of monoclinic $WO_3$, which is in excellent agreement with PXRD spectra.

It is well documented that the surface species deposited are highly dependent on the pzc (point of zero charges) of the support and the initial concentration of precursors of tungsten [33]. Polymeric tungsten species are deposited as the pH decreases below 4. In line with Ross-Medgaarden's [32] findings, the pzc of the support increases as the interfacial concentration of polymeric tungsten species decreases. Polymeric species are deposited on the acid-modified surface of titania through electrostatic forces involving several bridging and terminal hydroxo groups [32]. Upon calcination, polymeric species are transformed into octahedrally coordinated structures [34].

It is reasonable to assume that hydrogen bonds through hydroxo species are transformed into coordinative surface bonds. Moreover, it could also be assumed that these coordinative bonds are more stable in the glycerol oxy-dehydration harsh conditions, thereby prolonging the durability of such catalysts.

In the literature, coordinatively unsaturated wolframyl species containing W=O bonds acted as Lewis acid centers, while the same coordinatively unsaturated terminal groups in contact with titania acted as Bronsted acid centers [35,36]. The sustained presence of Lewis acid sites is related to the presence of isolated crystalline $WO_3$, whereas the formation of polytungstate species in contact with titania or silica concomitantly led to the increase in Bronsted acid centers.

**2. Effect of Solvent Mixture, $WO_3$ Percentage, LHSV and Glycerol Content in Catalytic Oxy-dehydration of Glycerol and Stability of Catalyst Performance**

Fig. 5 shows the catalytic performance for 2 h and 12 h in the oxy-dehydration of glycerol over 15%$WO_3$-$cSiO_2$-$TiO_2$ catalysts prepared with various solvents: Oxalic acid +acidified water (OA imp. W), Oxalic acid +acidified water/ethyl alcohol (50 : 50 v/v) mixture (OA imp. W/EA), Oxalic acid +acidified alcohol (OA imp. EA), without oxalic acid in acidified water alone (Imp. W). The acrolein, albeit small propanal, acetaldehyde, and acetic acid are detected in liquefiable condensates. Aldehydes and acrolein, respectively, are considered to be indicative of Lewis and Brønsted type acid sites' products. In terms of the acrolein selectivity and condensable' percentages, the catalysts prepared in an oxalic acid +acidified water/ethyl alcohol (50 : 50 v/v) mixture (OA imp. W/EA) exhibit higher selectivity and condensable percentages than other catalysts. The order of resistance to the deactivation of 15%$WO_3$-$cSiO_2$-$TiO_2$ prepared in various solvent mixtures after 12-hour long time on stream tests was as follows: (OA imp. W/EA)>(OA imp. EA)>(OA imp. W)>(Imp W) as shown in Fig. S8.

From $NH_3$-TPD results (see Table 1), 15%$WO_3$-$cSiO_2$-$TiO_2$ catalysts had the highest concentrations of total and medium strength

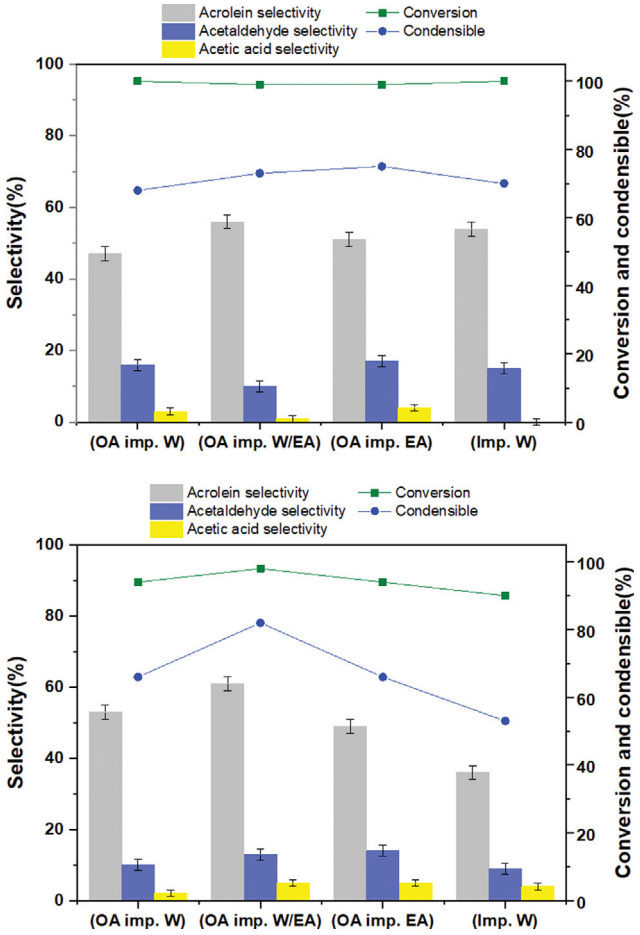


**Fig. 5. Catalytic performance in the oxy-dehydration of glycerol over 15%$WO_3$-($cSiO_2$)-$TiO_2$ catalysts prepared under various impregnation conditions first 2 h (left) and after 12 h TOS (right).**

acid sites. High concentration of medium strength acidity resulted in high oxy-dehydration activity. DRIFT analysis showed a maximum of B/(B+L) ratios at these concentrations too (see also Fig. S5). As a result of 12 h TOS study shown in Fig. 8 (right), major changes in the catalytic activities are depicted on the 15%$WO_3$-$cSiO_2$-$TiO_2$ catalyst. While acetaldehyde is obtained as the main by-product in all $WO_3$ loadings, higher amounts of acetaldehyde are observed only in 10% and 15% loaded samples (Fig. 6). Besides, liquid hourly space velocity (LHSV) and stability studies are carried out on 15%$WO_3$-($cSiO_2$)-$TiO_2$ (OA imp W/EA) since there is no significant increase in activity on 15%$WO_3$ loading and the amount of condensable product decreased too.

The progress of the steady state reaction with various LHSVs in the range of 4.7 to 18.8 $h^{-1}$ was carried out over 15%$WO_3$-$TiO_2$ catalyst with varying glycerol content (between 10% and 40% w/w in water), as shown in Fig. 7 (see also Fig. S9(a), (b) and (c) in supplementary file).

Changes in conversion and selectivity with respect to LHSVs for constant 10% glycerol content are depicted in Fig. 7. Glycerol conversion decreased from 100% at 4.7 $h^{-1}$ down to 48% at 18.8 $h^{-1}$, whereas the acrolein selectivity increased from 54% at 4.7 $h^{-1}$ up to 95% at 18.8 $h^{-1}$. This counteracting trend is explained by the

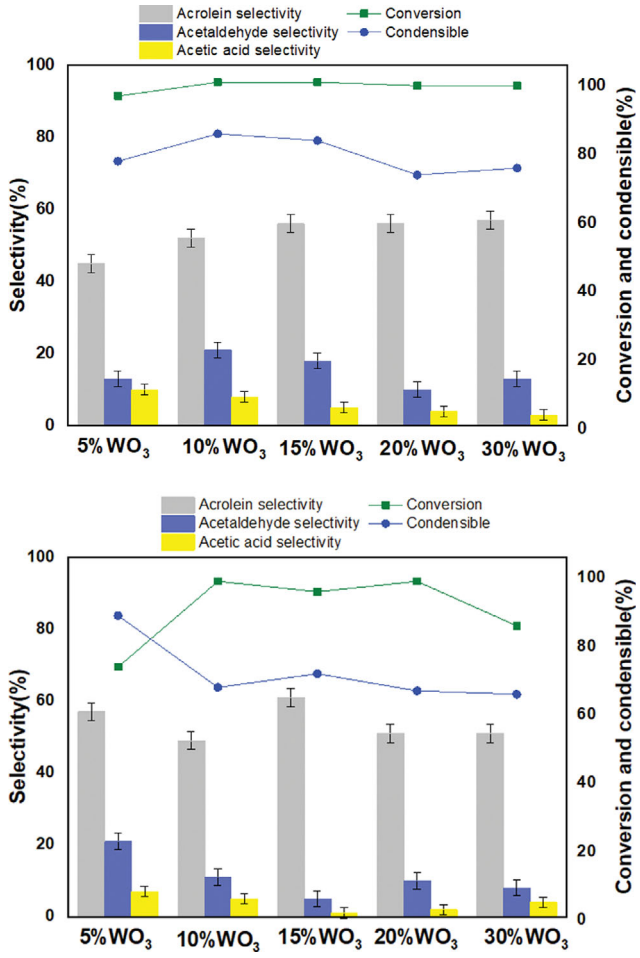


**Fig. 6. Reaction results of 5, 10, 15, 20 and 30%$WO_3$-($cSiO_2$)-$TiO_2$ (OA imp. W/EA) samples first 2 h (left) and after 12 h TOS (right)).**

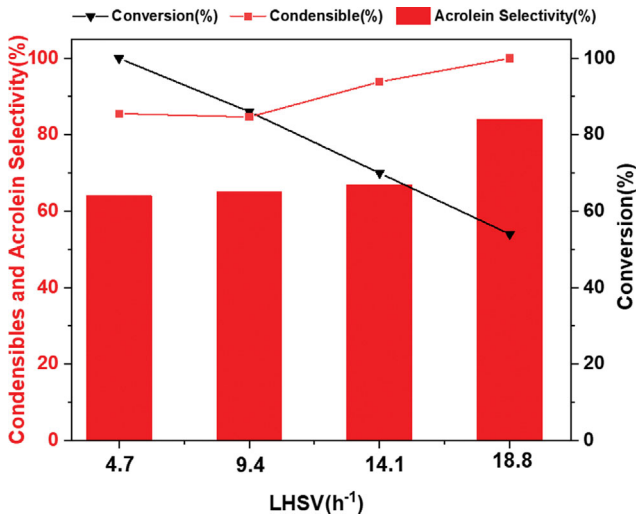


**Fig. 7. Glycerol dehydration reaction over 15%$WO_3$-$TiO_2$ catalyst with varying LHSVs for 10%wt glycerol content.**

decrease in the consecutive acrolein-consuming reactions leading to small molecules, such as, CO and formaldehyde, acetaldehyde.

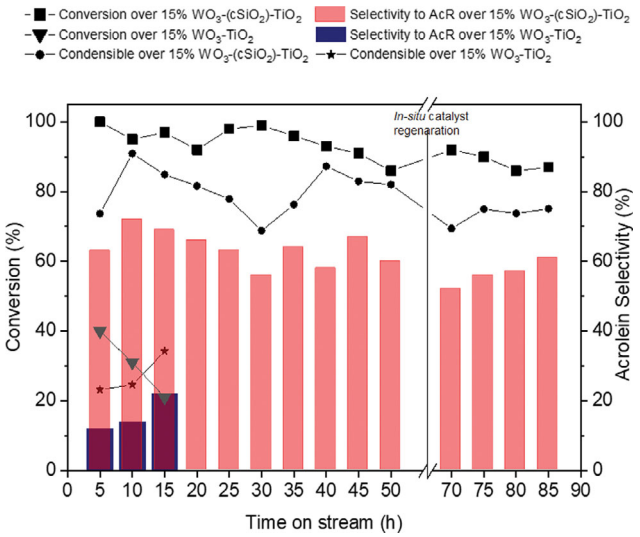


**Fig. 8. Progress of activity and selectivity to acrolein as a function of time-on-stream over 15%$WO_3$-$TiO_2$ with/without $cSiO_2$ depicted in total 75-h long time-on-stream.**

In addition to the increase in acrolein selectivity with increasing LHSV, glycerol conversion decreased due to lower contact times. Additionally, high LHSV favors the acrolein selectivity, probably not being able to further reaction, leading to heavier by-products due to short contact times. This phenomenon is also reported by Cavani et al. [37,38].

As the LHSVs increased from 4.7 to 18.8 $h^{-1}$, the increase in acrolein selectivity occurred in parallel with carbon balance improvement and the concomitant increase in the amounts of condensables [35]. The acrolein concentration increased along with LHSV and its maximum selectivity was 94% for 10% glycerol feed concentration at 18.8 $h^{-1}$. Similar counteracting trends are observed for the other glycerol feed concentrations as shown Fig. 7, S9(a), S9(b) and S9(c). A slight decrease in glycerol conversion from 10% to 40% glycerol content at lower LHSVs is explained by the decrease of the active sites by preferential adsorption of glycerol, thus enhancing side product [36].

The glycerol is converted at near complete conversions at low glycerol concentrations and low LHSVs, whereas acrolein is also subjected to further reactions with glycerol or oligomerisations, thereby lowering acrolein selectivity. On the other hand, at higher space velocities and high glycerol concentrations, glycerol conversion and consecutive reactions are retarded and acrolein selectivity increased up to 94%.

Glycerol is prone to further side reactions at higher contact times. However, acrolein is less reactive in comparison to glycerol and thus less prone to side reactions. This trend is also reported in the literature [39,40]. The glycerol content by weight and contact time in reactions have a significant influence on the catalytic activity and selectivity.

### 3. Catalyst Stability

Progress of activity and selectivity to acrolein as a function of time-on-stream over 15%$WO_3$-$TiO_2$ with and without $cSiO_2$ are investigated and depicted in Fig. S8 and Fig. 8, respectively. 15%$WO_3$

loaded catalysts (OA imp. W/EA) with $cSiO_2$ resulted in an average 60% acrolein yield at the end of 12 h (Fig. S8). In this respect, it can be argued that the catalyst with 15%$WO_3$-$TiO_2$ demonstrated the highest resistance to deactivation with an optimum B/(B+L) ratio of 0.74 and a medium strength acid concentration of 1437 μmol $NH_3$/g. Similar dependence of product selectivity and activity on acid sites and distribution was observed by Chieregato et al. [41] and Feng et al. [42].

From Fig. 8, the catalytic stability over the 15%$WO_3$-$TiO_2$ catalyst with $cSiO_2$ is found to be much higher than that of the 15%$WO_3$-$TiO_2$ catalyst without $cSiO_2$. After 15 hours of time-on-stream over 15%$WO_3$-$TiO_2$ catalyst without $cSiO_2$, conversion of glycerol decreased from an average 40% after 5 hours of on-stream to 21% at 15 hours of on-stream, selectivity changed from 13 to 24%. In the first 50-h of time-on-stream over 15%$WO_3$-$cSiO_2$-$TiO_2$ catalyst, glycerol conversion is on a slow decreasing trend from 100% to 86%, selectivity to acrolein is changed between 60 and 72%. Enhancement in the catalytic activity and stability by the addition of colloidal silica on the $WO_3$-$TiO_2$ catalyst system is proven for glycerol oxy-dehydration reaction as depicted in Fig. 8.

The beneficial effect of the addition of silica creating an additional surface area and porosity is well demonstrated in the literature [16]. Dubois et al. [43,44] studied the meso and macropores' effect on tungsten oxide supported over various oxides, such as $TiO_2$, and $SiO_2$. They claimed that the presence of pore volume higher than 0.3 $cm^3$/g and a volumetric ratio of macro to mesopores bigger than 0.5 was required to maintain high catalytic activity in the dehydration of glycerol.

The poor stability of W/$ZrSiO_2$ catalysts is claimed to be due to the presence of small mesopores (4.2 nm) leading to quick pore clogging due to the glycerol condensation [45]. 2.5W/$ZrO_2$ catalyst with larger mesopores (9.9 nm and pore volume 0.27 $cm^3$/g) maintained over 90% activity after 120 h of time-on-stream. The optimization of pore structure led to the sustained performance in glycerol dehydration.

In this study, we amply demonstrated that the addition of silica has benefits over the catalytic activity and stability. In Table 1, we proved that the 15%$WO_3$-$cSiO_2$-$TiO_2$ catalyst had a surface area of 6 fold higher than that of 15%$WO_3$-$TiO_2$ catalyst without $cSiO_2$. 15%$WO_3$-$cSiO_2$-$TiO_2$ catalyst had a pore volume of tenfold higher than that of the 15%$WO_3$-$TiO_2$ catalyst without $cSiO_2$. Similarly, 15%$WO_3$-$cSiO_2$-$TiO_2$ catalyst-provided B/(B+L) ratio of 0.74 and medium strength acidity of 1437 (μmoles $NH_3$/g). These two prominent factors, namely, B/(B+L) ratio and medium strength acidity, along with larger pore width (of 6.66 nm) resulted in the better yields and sustained activity.

*In-situ* regenerated catalyst underwent the same reaction conditions. As shown in Fig. 8, regenerated catalyst recovered high conversion and selectivity to acrolein for another 25 h. A similar slight deactivating trend was observed in *in-situ* regenerated 15%$WO_3$-$TiO_2$ sample. Moreover, the stability of active phases was also demonstrated by further XRD, XPS and performance tests. In Fig. 9, we studied the thermogravimetric behavior of 15%$WO_3$-$TiO_2$ samples with and without $cSiO_2$ after 15 and 50 h long time-on-streams. We found that carbonaceous deposits are all the same in terms of onset of oxidation temperatures. The onset of oxidation is only 50 degrees above the operating conditions. The carbonaceous deposits can easily be oxidized and hence spent catalysts can be regenerated without obliging high temperatures that might cause structural changes in regenerated catalysts.

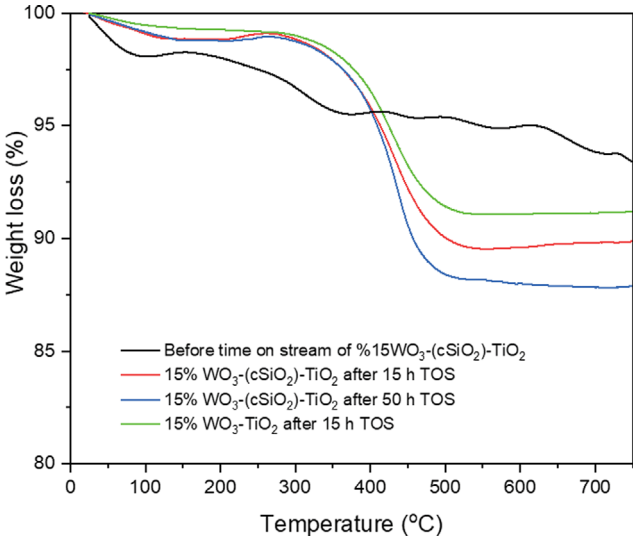


**Fig. 9. TGA plots of fresh and used 15%$WO_3$-($cSiO_2$)-$TiO_2$ catalysts after 50-h time-on-stream (TOS).**

## CONCLUSIONS

15%$WO_3$-$cSiO_2$-$TiO_2$ catalysts are very efficient and stable for the direct conversion of glycerol into acrolein. The key to the stable and selective conversions of glycerol to acrolein is that $WO_3$ on $cSiO_2$-$TiO_2$ catalysts show high concentrations of Brønsted acid and Lewis acid sites, an appropriate ratio of B/(B+L) being around 0.7, the highest value of pore volume, and diameter (ca. 6.7 nm). The solvent mixture used in the preparation of tungsten oxide over titania influences the catalytic activity and stability of the prepared catalysts. The oxalic acid acidified water plus ethyl alcohol solvent mixture in the synthesis of $WO_3$-$TiO_2$ results in favor of the medium strength and total surface acidity of the catalysts. High acrolein yields (60-70%) lasting at least 50 h time-on-stream at 300 °C over 15%$WO_3$-$cSiO_2$-$TiO_2$ are as promising as those reported in the literature. The increase in LHSV yields a considerable rise in the acrolein selectivity (up to 94%) over 15%$WO_3$-$cSiO_2$-$TiO_2$ catalyst. The most significant effect of changing solvent mixture in the impregnation stage is observed in the acid strength distribution and acid concentration. Consequent changes are observed not only in the acrolein selectivity but also in the stability of catalyst performance too. These three prominent factors, namely, B/(B+L) ratio and medium strength acidity, along with larger pore width (of 6.66 nm) result in better yields and prolonged activity.

## ACKNOWLEDGEMENTS

This work was supported by the Scientific and Technological Research Council of Turkey (TUBITAK) grant numbers 119M433 and 118C143.

## SUPPORTING INFORMATION

Additional information as noted in the text. This information is available via the Internet at http://www.springer.com/chemistry/journal/11814.

## REFERENCES INCORRECT FORMAT. PLEASE FOLLOW THE GUIDE


1. OECD-FAO *OECD-FAO Agricultural Outlook 2021-2030*, ISBN 978-92-5-134608-2 (2021).
2. A. Corma, G. W. Huber, L. Sauvanaud and P. O'Connor, *J. Catal.*, **257**, 163 (2008).
3. M. Pagliaro and M. Rossi, The Future of Glycerol: RSC Publishing, Chapter 7 Dehydration, ISBN 9781849730464 (2010).
4. M. Checa, S. Nogales-Delgado, V. Montes and J. M. Encinar, *Catalysts*, **10**, 1 (2020).
5. S. T. Wu, Q. M. She, R. Tesser, M. D. Serio and C. H. Zhou, *Catal. Rev. - Sci. Eng.*, **62**, 481 (2020).
6. D. Sun, Y. Yamada, S. Sato and W. Ueda, *Green Chem.*, **19**, 3186 (2017).
7. S. Chozhavendhan, G. Karthiga Devi, B. Bharathiraja, R. Praveen Kumar and S. Elavazhagan, *Assessment of crude glycerol utilization for sustainable development of biorefineries*, Elsevier Inc. (2020).
8. M. Dalil, D. Carnevali, J. L. Dubois and G. S. Patience, *Chem. Eng. J.*, **270**, 557 (2015).
9. L. Shen, H. Yin, A. Wang, Y. Feng, Y. Shen, Z. Wu and T. Jiang, *Chem. Eng. J.*, **180**, 277 (2012).
10. I. Martinuzzi, Y. Azizi, O. Zahraa and J. P. Leclerc, *Chem. Eng. Sci.*, **134**, 663 (2015).
11. I. Martinuzzi, Y. Azizi, J. F. Devaux, S. Tretjak, O. Zahraa and J. P. Leclerc, *Chem. Eng. Sci.*, **116**, 118 (2014).
12. C. A. G. Quispe, C. J. R. Coronado J. A. Carvalho, *Renew. Sustain. Energy Rev.*, **27**, 475 (2013).
13. I. Pala-Rosas, J. L. Contreras, J. Salmones, B. Zeifert, R. López-Medina, J. Navarrete-Bolaños, S. Hernández-Ramírez, J. Pérez-Cabrera and A. A. Fragoso-Montes De Oca, *Catalysts*, **11**, 1 (2021).
14. I. Pala Rosas, J. Luis Contreras Larios, B. Zeifert and J. Salmones Blásquez, *Glycerine Prod. Transform. - An Innov. Platf. Sustain. Biorefinery Energy*, 1 (2019).
15. T. M. Neves, J. O. Fernandes, L. M. Lião, E. Deise da Silva, C. Augusto da Rosa and V. B. Mortola, *Micropor. Mesopor. Mater.*, **275**, 244 (2019).
16. E. Tsukuda, S. Sato, R. Takahashi and T. Sodesawa, *Catal. Commun.*, **8**, 1349 (2007).
17. A. Abdullah, A. Z. Abdullah, M. Ahmed, P. U. Okoye and M. Shahadat, *Can. J. Chem. Eng.*, 1 (2021).
18. B. Katryniok, S. Paul, M. Capron and F. Dumeignil, *ChemSusChem*, **2**, 719 (2009).
19. M. Dalil, D. Carnevali, M. Edake, A. Auroux, J. L. Dubois and G. S. Patience, *J. Mol. Catal. A Chem.*, **421**, 146 (2016.
20. M. Dalil, M. Edake, C. Sudeau, J. L. Dubois and G. S. Patience, *Appl. Catal. A Gen.*, **522**, 80 (2016).
21. C. Hulteberg, A. Leveau and J. G. M. Brandin, *Top. Catal.*, **60**, 1462 (2017).
22. M. Massa, A. Andersson, E. Finocchio, G. Busca, F. Lenrick and L. R. Wallenberg, *J. Catal.*, **297**, 93 (2013).
23. Z. Babaei, A. Najafi Chermahini and M. Dinari, *J. Colloid Interface Sci.*, **563**, 1 (2020).
24. R. Liu, T. Wang, D. Cai and Y. Jin, *Ind. Eng. Chem. Res.*, **53**, 8667 (2014).
25. S. Musić, N. Filipović-Vinceković and L. Sekovanić, *Brazilian J. Chem. Eng.*, **28**, 89 (2011).
26. X. Liu, H. Chen, X. Wu, L. Cao, P. Jiang, Q. Yu and Y. Ma, *Catal. Sci. Technol.*, **9**, 3711 (2019).
27. M. Mokhtarifar, D. T. Nguyen, M. V. Diamanti, R. Kaveh, M. Asa, M. Sakar, M. P. Pedeferri and T. O. Do, *New J. Chem.*, **44**, 20375 (2020).
28. C. Liebig, S. Paul, B. Katryniok, C. Guillon, J. L. Couturier, J. L. Dubois, F. Dumeignil and W. F. Hoelderich, *Appl. Catal. B Environ.*, **132-133**, 170 (2013).
29. H. Yang, D. Zhang and L. Wang, *Mater. Lett.*, **57**, 674 (2002).
30. J. H. Pan and W. I. Lee, *Chem. Mater.*, **18**, 847 (2006).
31. A. Tagliaferro, M. Rovere, E. Padovano, M. Bartoli M. Giorcelli, *Nanomaterials*, **10**, 1 (2020).
32. E. I. Ross-Medgaarden and I. E. Wachs, *J. Phys. Chem. C*, **111**, 15089 (2007).
33. G. D. Panagiotou, T. Petsi, K. Bourikas, C. Kordulis and A. Lycourghiotis, *J. Catal.*, **262**, 266 (2009).
34. A. M. Hirt, *J. Phys. Chem.*, **95**, 991 (1991).
35. P. Lauriol-Garbay, J. M. M. Millet, S. Loridant, V. Bellire-Baca and P. Rey, *J. Catal.*, **280**, 68 (2011).
36. X. C. Jiang, C. H. Zhou, R. Tesser, M. Di Serio, D. S. Tong and J. R. Zhang, *Ind. Eng. Chem. Res.*, **57**, 10736 (2018).
37. F. Cavani, S. Guidetti, L. Marinelli, M. Piccinini, E. Ghedini and M. Signoretto, *Appl. Catal. B Environ.*, **100**, 197 (2010).
38. T. Ma, Z. Yun, W. Xu, L. Chen, L. Li, J. Ding and R. Shao, *Chem. Eng. J.*, **294**, 343 (2016).
39. M. Akizuki and Y. Oshima, *Ind. Eng. Chem. Res.*, **51**, 12253 (2012).
40. A. Talebian-Kiakalaieh and N. A. S. Amin, *Chem. Eng. Trans.*, **56**, 655 (2017).
41. A. Chieregato, M. D. Soriano, F. Basile, G. Liosi, S. Zamora, P. Concepción, F. Cavani and J. M. López Nieto, *Appl. Catal. B Environ.*, **150-151**, 37 (2014).
42. X. Feng, Y. Yao, Q. Su, L. Zhao, W. Jiang, W. Ji and C. T. Au, *Appl. Catal. B Environ.*, **164**, 31 (2015).
43. J.-L. Dubois, K. Okumura, Y. Kobayash and R. Hiraoka, Improved Process of Dehydration Reactions, WO2013017904 (2013).
44. J.-L. Dubois, Method for Synthesis of Acrolein from Glycerol US 2010/0274038A1 (2010).
45. R. Znaiguia, L. Brandhorst, N. Christin, V. Bellière Baca, P. Rey, J. M. M. Millet and S. Loridant, *Micropor. Mesopor. Mater.*, **196**, 97 (2014).

# Supporting Information

# Sustainable production of acrolein over highly stable and selective $WO_3$ over $SiO_2$-$TiO_2$ catalysts

**Ismail Boz†, Mehtap Safak Boroglu, Yasar Zengin, and Busra Kaya**

Istanbul University-Cerrahpaşa, Faculty of Engineering, Chemical Engineering Department, Avcılar, 34320 Istanbul, Turkey
(*Received 1 October 2022 • Revised 11 February 2023 • Accepted 27 February 2023*)

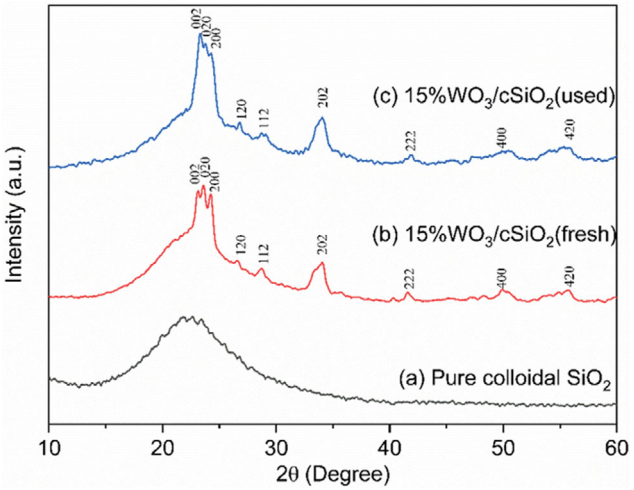


**Fig. S1. XRD patterns of (a) pure colloidal $cSiO_2$ samples, (b) fresh 15%$WO_3$-c-$SiO_2$, and (c) used 15%$WO_3$-c-$SiO_2$ for 8 hours of oxy-dehydration reaction.**

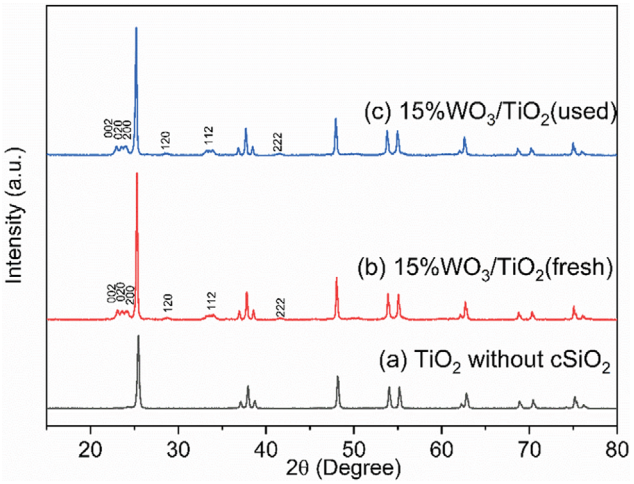


**Fig. S2. XRD patterns of (a) anatase $TiO_2$ samples, (b) fresh 15%$WO_3$-$TiO_2$, and (c) used 15%$WO_3$-$TiO_2$ for 8 hours of dehydration reaction.**

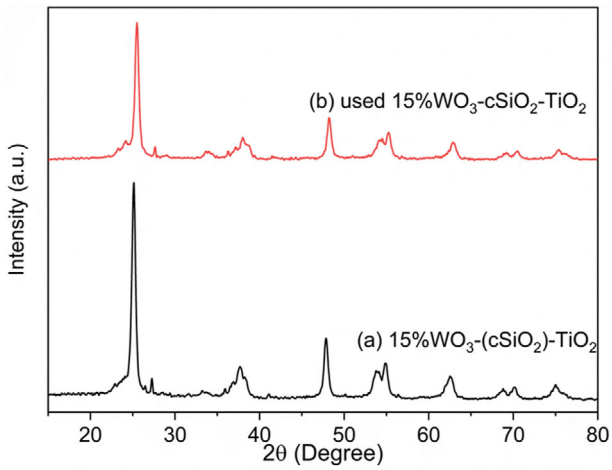


**Fig. S3. XRD patterns of samples (a) fresh 15%$WO_3$-($cSiO_2$)-$TiO_2$ and (b) used 15%$WO_3$-($cSiO_2$)-$TiO_2$ for 8 hours of oxy-dehydration reaction.**

**Table S1. Atomic percentages determined by XPS analysis over 15%$WO_3$-($cSiO_2$)-$TiO_2$ fresh (A) and spent (B) catalysts**

(A) Elemental ID and Quantification

| Deconvoluted peak name | Peak BE | FWHM (ev) | Area(P) CPS.ev | Atomic % |
|---|---|---|---|---|
| O1s Scan A | 529.41 | 1.24 | 11,432.64 | 49.95 |
| O1s Scan B | 531.17 | 2.37 | 4,031.26 | 17.64 |
| O1s Scan C | 531.93 | | | |
| W4f7 Scan A | 33.37 | 1.45 | 183.60 | 0.27 |
| W4f7 Scan B | 34.90 | 1.42 | 1,553.89 | 2.30 |
| W4f7 Scan C | 36.50 | 1.47 | 1,137.87 | 1.68 |
| Si2p3 Scan A | 101.82 | 1.83 | 221.95 | 3.53 |
| Ti2p3 Scan A | 458.18 | 1.19 | 9,121.63 | 24.63 |

(B) Elemental ID and Quantification

| Deconvoluted peak name | Peak BE | FWHM (ev) | Area(P) CPS.ev | Atomic % |
|---|---|---|---|---|
| O1s Scan A | 529.09 | 1.25 | 10,488.40 | 42.88 |
| O1s Scan B | 530.47 | 1.92 | 3,255.72 | 13.24 |
| O1s Scan C | 531.93 | 1.75 | 3,253.98 | 13.33 |
| W4f7 Scan A | 34.06 | 1.39 | 480.62 | 0.66 |
| W4f7 Scan B | 35.95 | 1.19 | 2,150.31 | 2.98 |
| W4f7 Scan C | 36.95 | 1.23 | 1,674.21 | 2.32 |
| Si2p3 Scan A | 102.57 | 2.56 | 313.16 | 4.67 |
| Ti2p3 Scan A | 457.92 | 1.18 | 7,884.53 | 19.92 |

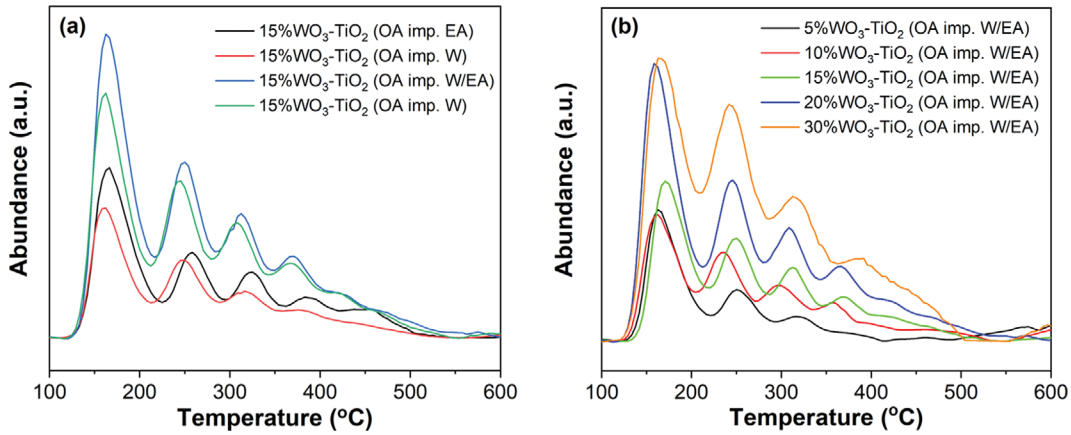


**Fig. S4. Ammonia-TPD curves of the catalysts 15%$WO_3$-(c$SiO_2$)-$TiO_2$ prepared with various solvent mixtures (a) and 5-30%$WO_3$-(c$SiO_2$)-$TiO_2$ samples (OA imp W/EA) (b).**

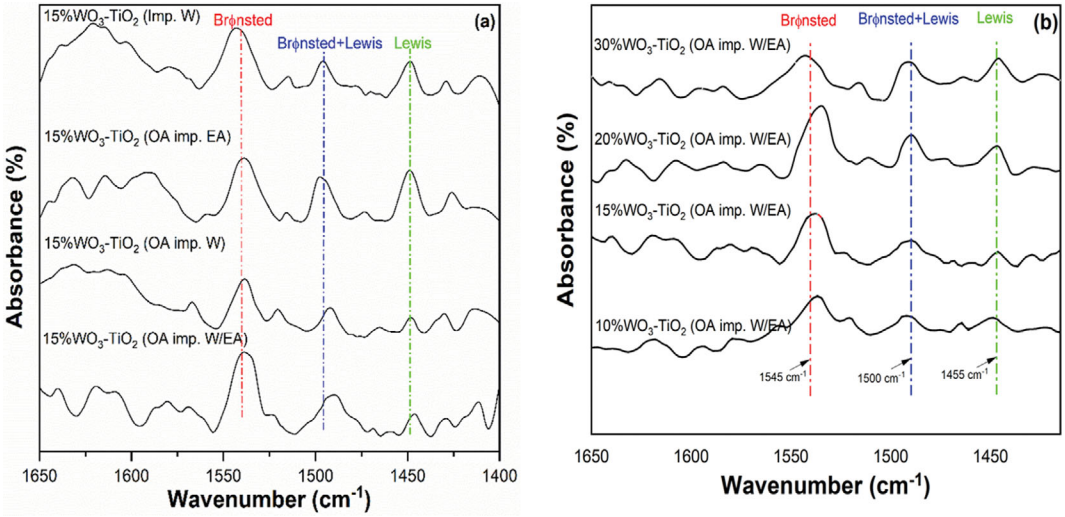


**Fig. S5. DRIFT spectra of the catalysts 15%$WO_3$-(c$SiO_2$)-$TiO_2$ prepared with various solvent mixtures (a) and 10-30%$WO_3$-(c$SiO_2$)-$TiO_2$ samples (OA imp W/EA) (b).**

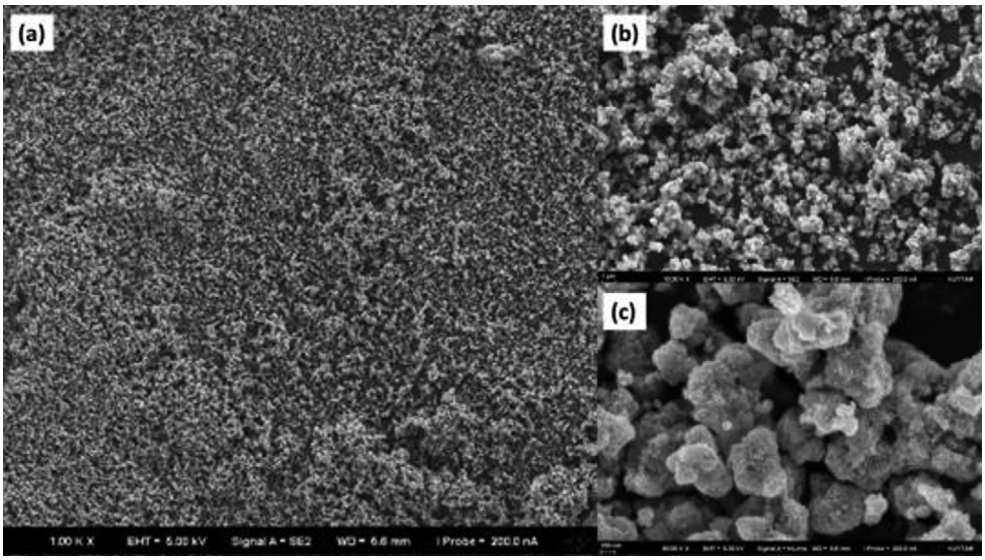


**Fig. S6. SEM pictures of 15%$WO_3$-$TiO_2$ (OA imp. W/EA).**

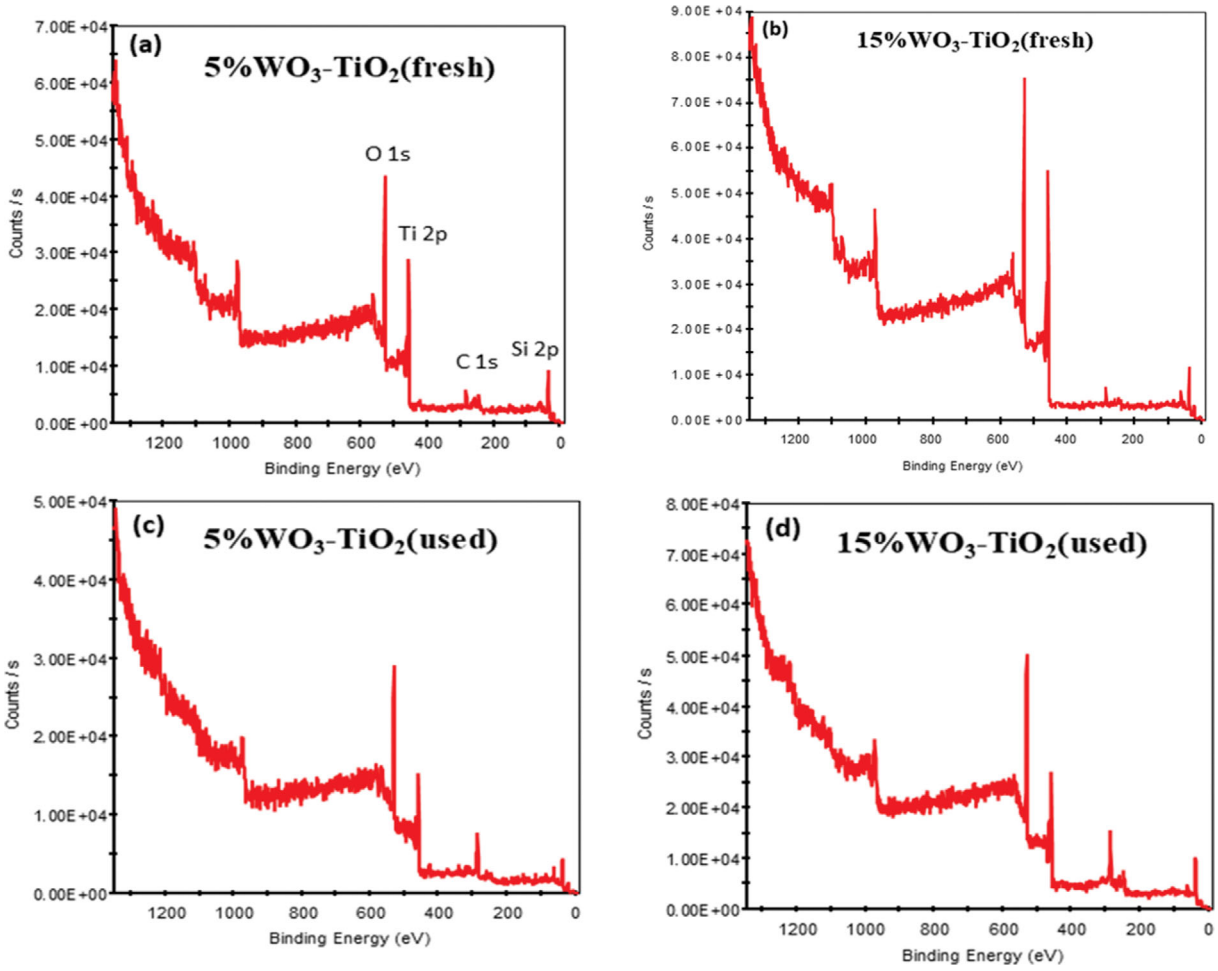


Fig. S7. General scan XPS spectra of 5% and 15%$WO_3$-$TiO_2$ (OA imp. W/EA).

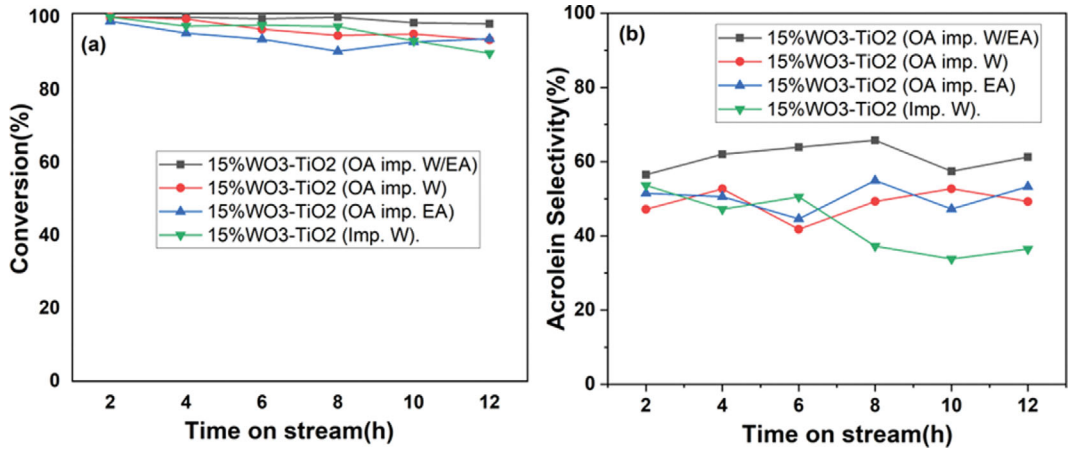


Fig. S8. Progress of activity and selectivity to acrolein as a function of time on stream over 15%$WO_3$-$TiO_2$ prepared with different solutions depicted in total 12 h long time on stream.

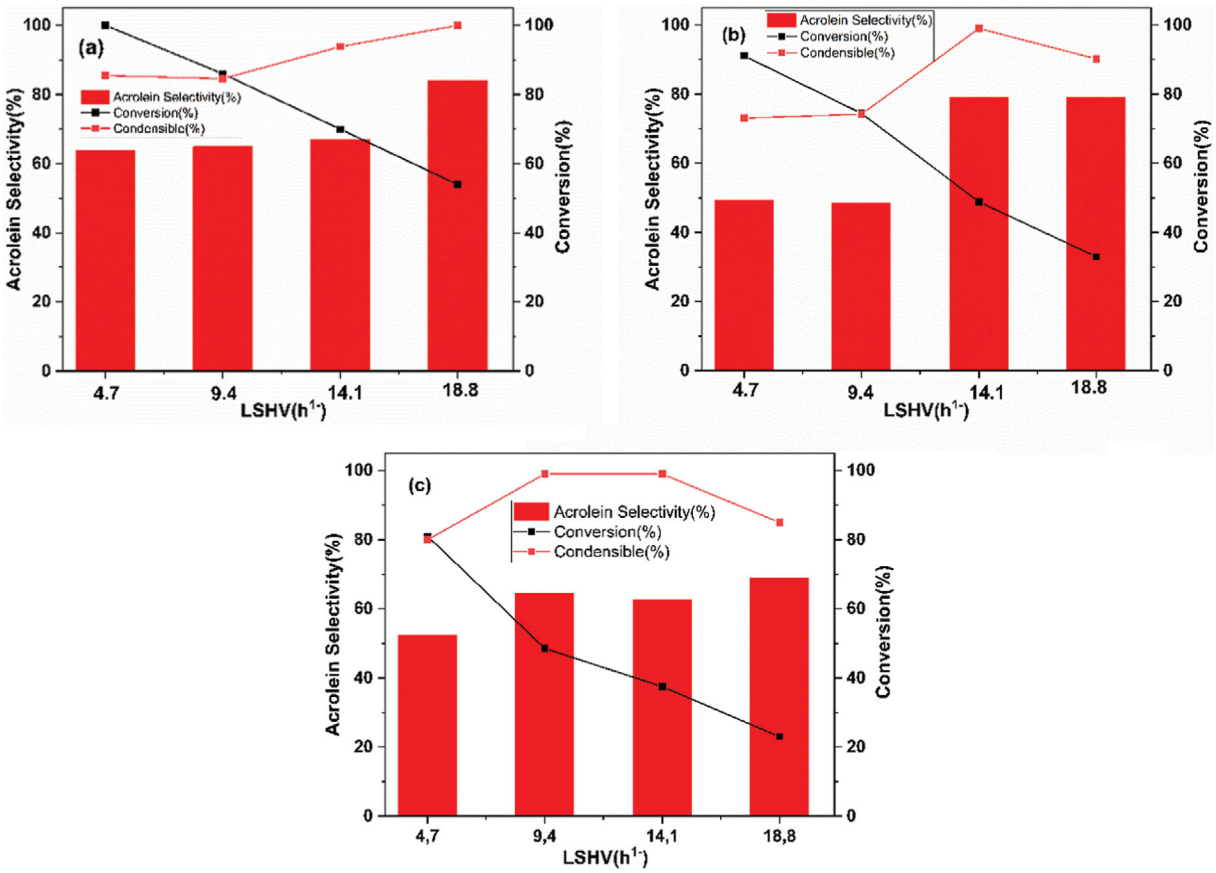


**Fig. S9. Glycerine dehydration reaction over 15%$WO_3$-$TiO_2$ catalyst with 20%wt (a), 30%wt (b) and 40%wt (c) glycerine contents LSHV.**